Temporal Evolution of a Geostrophic Current under Sea Ice: Analytical and Numerical Solutions

HENGLING LENG,[a,b,c] MICHAEL A. SPALL,[d] AND XUEZHI BAI[a,b]

[a] *Key Laboratory of Marine Hazards Forecasting, Ministry of Natural Resources, Hohai University, Nanjing, China*
[b] *College of Oceanography, Hohai University, Nanjing, China*
[c] *State Key Laboratory of Satellite Ocean Environment Dynamics, Second Institute of Oceanography, Ministry of Natural Resources, Hangzhou, China*
[d] *Woods Hole Oceanographic Institution, Woods Hole, Massachusetts*

(Manuscript received 28 October 2021, in final form 17 February 2022)

ABSTRACT: A simplified quasigeostrophic (QG) analytical model together with an idealized numerical model are used to study the effect of uneven ice–ocean stress on the temporal evolution of the geostrophic current under sea ice. The tendency of the geostrophic velocity in the QG model is given as a function of the lateral gradient of vertical velocity and is further related to the ice–ocean stress with consideration of a surface boundary layer. Combining the analytical and numerical solutions, we demonstrate that the uneven stress between the ice and an initially surface-intensified, laterally sheared geostrophic current can drive an overturning circulation to trigger the displacement of isopycnals and modify the vertical structure of the geostrophic velocity. When the near-surface isopycnals become tilted in the opposite direction to the deeper ones, a subsurface velocity core is generated (via geostrophic setup). This mechanism should help understand the formation of subsurface currents in the edge of Chukchi and Beaufort Seas seen in observations. Furthermore, our solutions reveal a reversed flow extending from the bottom to the middepth, suggesting that the ice-induced overturning circulation potentially influences the currents in the deep layers of the Arctic Ocean, such as the Atlantic Water boundary current.

KEYWORDS: Arctic; Sea ice; Channel flows; Vertical motion; Ekman pumping; Idealized models; Quasigeostrophic models

1. Introduction

The ocean currents in the Arctic, especially in submarine canyons or along the edge of shelf seas, have some different characteristics from those in mid- and low-latitude oceans, such as the velocity structure and seasonality. Using data from a year-long array spanning the shelf break and upper-slope of the Chukchi Sea, Li et al. (2019) found that the Chukchi Slope Current (a newly identified northwestward-flowing current along the Chukchi slope, see Corlett and Pickart 2017) is surface intensified in summer and fall, while it is dominated by a subsurface velocity maximum (~100-m depth) during winter and spring (see the schematic in Fig. 1). In their velocity sections, the subsurface velocity maximum appears as a core surrounded by velocity contours and is thus referred to as a velocity core. A similar subsurface velocity core was also observed in the Barrow Canyon throughflow (Itoh et al. 2013; Weingartner et al. 2017), and the eastward Beaufort shelfbreak jet at 152°W (Nikolopoulos et al. 2009) and farther east to the vicinity of Mackenzie Canyon, Beaufort Sea (Lin et al. 2020). These observations suggest that the subsurface current is common in the edge of Chukchi and Beaufort Seas and is probably present in the other areas of the Arctic Ocean.

Recent numerical studies support the presence of the subsurface core in the Barrow Canyon throughflow (Spall et al. 2018; Leng et al. 2021) and the Chukchi Slope Current (Watanabe et al. 2017; Leng et al. 2021). In the model of Watanabe et al. (2017), the subsurface slope current (referred to as a "shelfbreak jet") appears to be related to the depression of upper isohalines on the shelf side due to shelf water intrusion. However, the model of Leng et al. (2021) implies that the changing structure of the slope current is likely to be dictated by the flow through Barrow Canyon. At present, it is unclear which factor dominates the structure of the slope current.

It seems likely that the slope current structure is related to sea ice, considering that the subsurface core occurs more frequently during ice-covered periods (Watanabe et al. 2017; Li et al. 2019; Leng et al. 2021). It has been demonstrated that the interaction between the ice and the surface current, dubbed the "ice–ocean governor," plays a significant role in regulating the speed and depth of the large-scale Beaufort Gyre in the Canada Basin (e.g., Meneghello et al. 2018a, 2020; Wang et al. 2019; Doddridge et al. 2019). Furthermore, the ice–ocean stress has also been suggested as an explanation for observed subsurface maxima in eddy kinetic energy in the interior Arctic Ocean—via impacts both on unstable growth of baroclinic instability and on finite-amplitude eddies (Meneghello et al. 2021). Nonetheless, little is known regarding the role of ice–ocean stress along the edge of Chukchi and Beaufort Seas, where the currents along the topography are suggested to be distinct from the gyre in the basin interior (Corlett and Pickart 2017; Watanabe et al. 2017; Spall et al. 2018). It is worth noting that the slope current is laterally sheared [see, e.g., Fig. 3 in Li et al. (2019) and Fig. 2 in Boury et al. (2020)] such that the Ekman pumping over the region should be large in ice-covered periods due to uneven ice–ocean stress. The

---

Corresponding author: Hengling Leng, hengling_leng@hotmail.com

DOI: 10.1175/JPO-D-21-0242.1

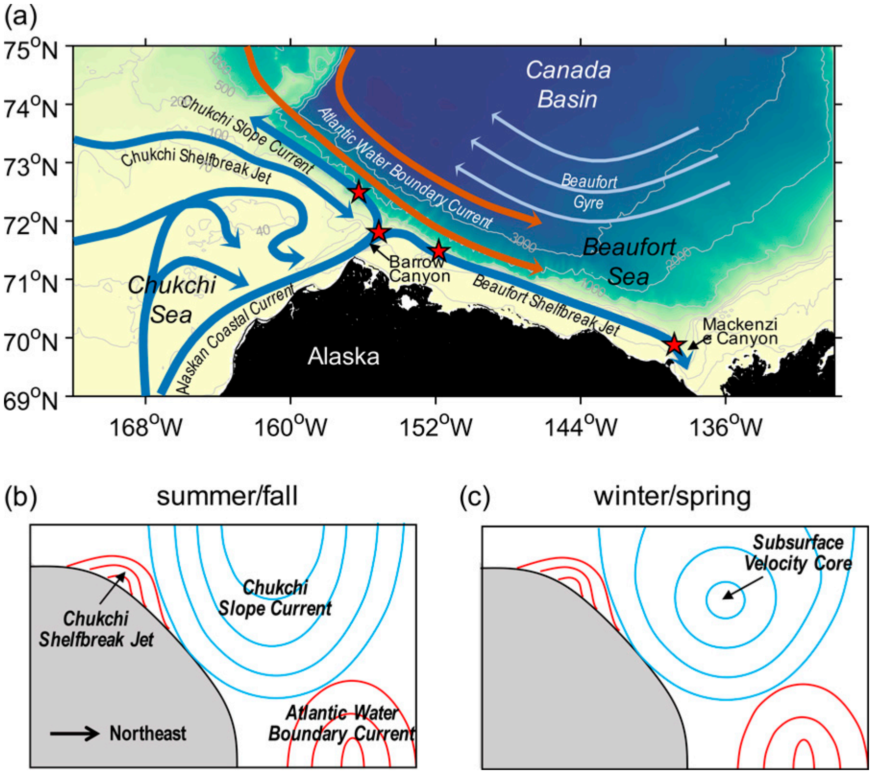

FIG. 1. (a) Schematic circulation of the Chukchi and Beaufort Seas and place names. The red stars mark the locations where a subsurface velocity core has been observed. (b),(c) Schematic summer/fall and winter/spring velocity structures in the region of Chukchi shelf break and slope. Blue contours indicate the northwestward Chukchi Slope Current, opposite to the southeastward flows (Chukchi shelfbreak jet and Atlantic Water boundary current) indicated by red contours.

observational study of Meneghello et al. (2018b) suggests that this is the case, although the altimetry-derived geostrophic velocity dataset used in their study is too coarse (0.25° × 0.75° resolution) to distinguish the slope current from the gyre.

These findings motivate us to establish a theoretical framework, not only to explain the formation of the subsurface velocity core seen in observations, but to clarify the effect of uneven ice–ocean stress on the evolution of the geostrophic current. The theoretical framework in this paper is on the basis of the quasigeostrophic (QG) formulation in combination with Ekman boundary conditions. We also set up an idealized numerical model to support the analytical results. The paper is organized as follows: section 2 describes the QG model and the idealized numerical model. Section 3 gives the analytical solutions. In section 4, we compare the analytical solutions to the numerical results and propose a mechanism for the overturning-induced modification of the geostrophic current. Finally, we summarize and discuss the findings of our work in section 5.

2. Analytical and numerical models

a. The QG model

The basic assumption in this study is that an initially surface-intensified, laterally sheared current will develop a subsurface maximum in velocity through ice–ocean stress and Ekman layer dynamics. The observational subsurface velocity core in the Chukchi Slope Current is of order 0.1 m s^{-1} and has a length scale of 10 km (Li et al. 2019). For the typical reference Coriolis parameter $f_0 = O(10^{-4})\ \mathrm{s}^{-1}$, the Rossby number is small (order 0.1) and thus the QG model is valid for theoretical analysis. We introduce the QG model on an f plane with consideration of a northward-flowing current through a meridional channel (Fig. 2). The channel is set in the Cartesian coordinate system, with a length of Y, a width of B, and a depth of H. The initial current is surface-intensified and laterally sheared, extending down to a depth of H_0, with a uniform width of l. Along-channel variations are assumed to be negligible ($\partial F/\partial y = 0$, F is any variable) so as to focus on the temporal evolution. The resulting simplified QG equations for the momentum, density, and continuity are given by

$$-f_0 v_g = -\frac{1}{\rho_0}\frac{\partial P}{\partial x}, \tag{1}$$

$$\frac{\partial v_g}{\partial t} + f_0 u = 0, \tag{2}$$

$$\frac{\partial \rho}{\partial t} + w\frac{\partial \overline{\rho}}{\partial z} = 0, \tag{3}$$

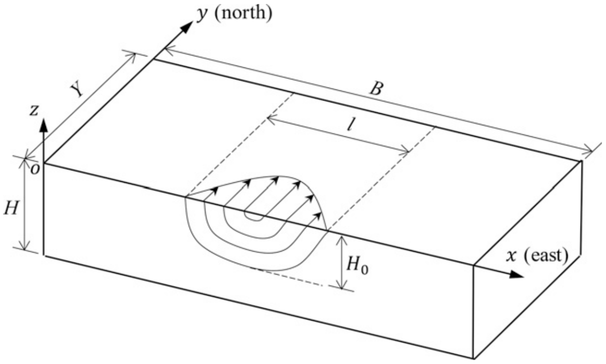

FIG. 2. Schematic channel for the analytical and numerical models; Y is the channel length, B is the channel width, and H is the channel depth. The initial current flowing northward along the channel is surface intensified and laterally sheared, with a depth of H_0 and a width of l.

$$\frac{\partial u}{\partial x} + \frac{\partial w}{\partial z} = 0, \tag{4}$$

where v_g (geostrophic) and u (ageostrophic) are along- and cross-channel velocities, with P being pressure, f_0 the Coriolis parameter, and ρ_0 the reference density; ρ is the varying density and is modified by vertical velocity w via advecting a background mean density gradient $\partial\overline{\rho}/\partial z$. We drop advection in the x direction in Eq. (3). This is because u is ageostrophic and hence small, and that this advects a perturbation density gradient, which is also small—making the term small compared to the vertical advection term. Note that the QG density and continuity equations are applicable for all depths, whereas the momentum equations are not valid in the surface boundary layer since the viscosity is not included.

Eliminating the time derivatives by combining Eqs. (1)–(4) gives a homogeneous form of the QG omega equation:

$$N^2\frac{\partial^2 w}{\partial x^2} + f_0^2\frac{\partial^2 w}{\partial z^2} = 0, \tag{5}$$

where $N^2 = -(g/\rho_0)(\partial\overline{\rho}/\partial z)$ is the square of the buoyancy frequency, and g is the gravitational acceleration. For details regarding the derivation of the omega equation, see Hoskins et al. (1978). This equation will be solved subject to boundary conditions on w at the surface, bottom, and lateral sides, which are described in detail in section 3a.

Equation (3) can be rewritten as

$$\frac{g}{\rho_0}\frac{\partial \rho}{\partial t} - N^2 w = 0. \tag{6}$$

If the buoyancy frequency is taken to be constant, partial derivative of Eq. (6) with respect to x gives

$$\frac{g}{\rho_0}\frac{\partial}{\partial t}\left(\frac{\partial \rho}{\partial x}\right) - N^2\frac{\partial w}{\partial x} = 0, \tag{7}$$

where $\partial\rho/\partial x$ can be replaced by $\partial v_g/\partial z$ according to the thermal wind relation:

$$f_0\frac{\partial v_g}{\partial z} = -\frac{g}{\rho_0}\frac{\partial \rho}{\partial x}, \tag{8}$$

then, Eq. (7) becomes

$$\frac{\partial}{\partial t}\left(\frac{\partial v_g}{\partial z}\right) = -\frac{N^2}{f_0}\frac{\partial w}{\partial x}. \tag{9}$$

Assuming $v_g \equiv 0$ as $z \to -\infty$, and integrating Eq. (9) vertically from $-\infty$ to $z = 0$, yields

$$\frac{\partial v_s}{\partial t} = -\frac{N^2}{f_0}\frac{\partial}{\partial x}\int_{-\infty}^{0} w\,dz, \tag{10}$$

where v_s is the surface geostrophic velocity. This equation indicates that the evolution of the geostrophic current depends on the lateral gradient of vertical velocity. Once v_s and w are resolved, the geostrophic velocity in the interior is determined by

$$\frac{\partial v_g}{\partial t} = \frac{\partial v_s}{\partial t} + \frac{N^2}{f_0}\frac{\partial}{\partial x}\int_{z}^{0} w\,dz. \tag{11}$$

b. *The idealized numerical model*

Following the analytical model, we set up a numerical channel on the f plane using the Massachusetts Institute of Technology general circulation model (MITgcm) (Marshall et al. 1997). The channel is configured on a 10 km (length) ×150 km (width) Cartesian grid with a uniform horizontal resolution of 2 km. The depth of the channel is 500 m and is divided into 48 vertical levels. The layer thickness increases gradually from 2 m at the top layer to 25 m at the bottom layer. Periodic boundary conditions are applied on the southern and northern boundaries so that along-channel variations are negligible (the model is approximately two dimensional). There is no drag at the bottom.

The model uses the nonlinear seawater state equation of Jackett and McDougall (1995) and nonlocal K-profile parameterization (KPP) scheme of Large et al. (1994). Horizontal viscosity is modified from the scheme of Leith (1996) to sense the divergent flow (Fox-Kemper and Menemenlis 2008). We set the nondimensional Leith biharmonic viscosity factor to be 1.5 for both the vorticity part and the divergence part. The ocean model is coupled to a variant of the viscous-plastic dynamic–thermodynamic sea ice model (Zhang and Hibler 1997) as described by Losch et al. (2010).

The numerical model is initialized with the temperature, salinity, and geostrophic velocity fields. We set the initial temperature to be 0°C throughout the channel and calculate the salinity from the temperature and density fields using the equation of state of seawater (the initial geostrophic velocity and density are given in section 4). The initial sea ice covers the whole domain with a uniform thickness of 1 m. We also input a constant downward shortwave radiation (20 W m^{-2}) and longwave radiation (180 W m^{-2}) (representative wintertime values in the Arctic) such that the sea ice is maintained.

3. Analytical solutions to the QG model

a. Solving the QG omega equation

1) SURFACE BOUNDARY CONDITION

The ice–ocean stress depends on the relative velocity between the ice and ocean and can be calculated using a quadratic drag law (e.g., Meneghello et al. 2020), $\boldsymbol{\tau} = \alpha\rho_0 C_{Di}|\mathbf{u}_{\text{ice}} - \mathbf{u}_s|(\mathbf{u}_{\text{ice}} - \mathbf{u}_s)$, where α is the sea ice concentration, C_{Di} is the dimensionless drag coefficient, $\mathbf{u}_{\text{ice}}$ is the ice velocity, and $\mathbf{u}_s$ is the surface geostrophic velocity. If the ice motion is assumed to be negligible, the ice–ocean stress can be simplified as a function of the surface geostrophic velocity. For the case that the current is flowing along the meridional channel, we need only consider the meridional ice–ocean stress:

$$\tau^y = -\alpha\rho_0 C_{Di} v_s^2, \tag{12}$$

which means that a northward surface velocity would give rise to a southward ice–ocean stress. Due to the presence of the lateral shear in the surface geostrophic velocity, the resulting ice–ocean stress is uneven. On the west side of the velocity maximum, the ice–ocean stress has a negative curl ($\partial\tau^y/\partial x < 0$) due to the positive velocity shear ($\partial v_s/\partial x > 0$). On the east side of the velocity maximum, the stress curl is positive ($\partial\tau^y/\partial x > 0$), corresponding to the negative velocity shear ($\partial v_s/\partial x < 0$). This yields a symmetrical distribution of Ekman downwelling and upwelling as illustrated in Fig. 3.

The vertical velocity in the surface boundary layer ($-\delta \le z \le 0$, δ is the boundary layer depth) is obtained by combining the Ekman horizontal velocity and the continuity equation. If the ice–ocean stress is nondivergent, we have

$$w = \left[1 - \exp\left(\frac{z}{D_E}\right)\cos\left(\frac{z}{D_E}\right)\right]w_E, \tag{13}$$

where D_E is the Ekman depth, and

$$w_E = \frac{1}{f_0\rho_0}\frac{\partial\tau^y}{\partial x} \tag{14}$$

is the Ekman pumping (note that zonal stress is neglected). It is appropriate to set $\delta = (\pi/2)D_E$, so that $w = w_E$ at $z = -\delta$. Namely, the Ekman pumping is treated as a boundary condition to drive the vertical motions in the interior.

2) INTERIOR SOLUTION

The vertical velocity in the interior ($-H \le z < -\delta$) is obtained by solving the QG omega equation [Eq. (5)]. Using the method of separation of variables with the following boundary conditions:

$$w(0, z) = 0,\ w(B, z) = 0,$$
$$w(x, -\delta) = w_E,\ w(x, -H) = 0,$$

we find an analytical solution:

$$w(x, z) = \sum_{k=1}^{\infty} a_k \sinh\left[\frac{k\pi N}{f_0 B}(z + H)\right]\sin\left(\frac{k\pi}{B}x\right), \tag{15}$$

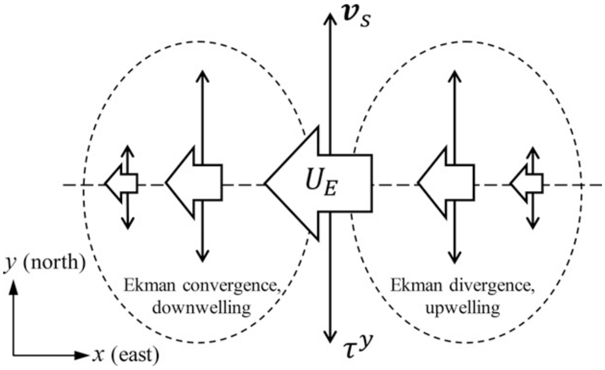

FIG. 3. Schematic showing a symmetrical distribution of Ekman downwelling and upwelling driven by ice–ocean stress curl. The ice motion is neglected and the northward geostrophic velocity v_s gives rise to the southward ice–ocean stress τ^y. The Ekman transport U_E driven by uneven ice–ocean stress is convergent on the west side and divergent on the east side.

with

$$a_k = \frac{2}{B\sinh\left[\frac{k\pi N}{f_0 B}(H - \delta)\right]}\int_0^B w_E(x)\sin\left(\frac{k\pi}{B}x\right)dx,\ k = 1, 2, 3, \ldots \tag{16}$$

b. Solving the evolution equation

By combining Eqs. (10) and (12)–(16) and replacing the quadratic ice–ocean stress with a linear drag,

$$\hat{\tau}^y = -\alpha\rho_0 C_{Di}\overline{V}v_s, \tag{17}$$

we derive a linear evolution equation for the surface geostrophic velocity (see the derivation in the appendix):

$$\frac{\partial v_s}{\partial t} - \overline{V}\mu\frac{\partial^2 v_s}{\partial x^2} = 0, \tag{18}$$

where $\overline{V}$ is the zonal average of the initial surface velocity, and $\mu = \alpha C_{Di}N^2 H_E/f_0^2$ is a parameter (H_E is the significant height of Ekman pumping). Note that Eq. (18) is of the same form as the heat (or diffusion) equation, where the coefficient $\overline{V}\mu$ can be regarded as a rate at which the surface geostrophic flow expands.

For the given initial velocity $v_s(x, 0)$, solving Eq. (18) by the method of separation of variables with Dirichlet boundary conditions $v_s(0, t) = v_s(B, t) = 0$ yields

$$v_s(x, t) = \sum_{k=1}^{\infty} c_k \exp\left(\frac{-k^2\pi^2}{B^2}\mu\overline{V}t\right)\sin\left(\frac{k\pi}{B}x\right), \tag{19}$$

with

$$c_k = \frac{2}{B}\int_0^B v_s(x, 0)\sin\left(\frac{k\pi}{B}x\right)dx,\ k = 1, 2, 3, \ldots \tag{20}$$

Since the surface geostrophic velocity $v_s(x, t)$ is known, we can calculate the ice–ocean stress $\tau^y(x, t)$ from Eq. (17), the

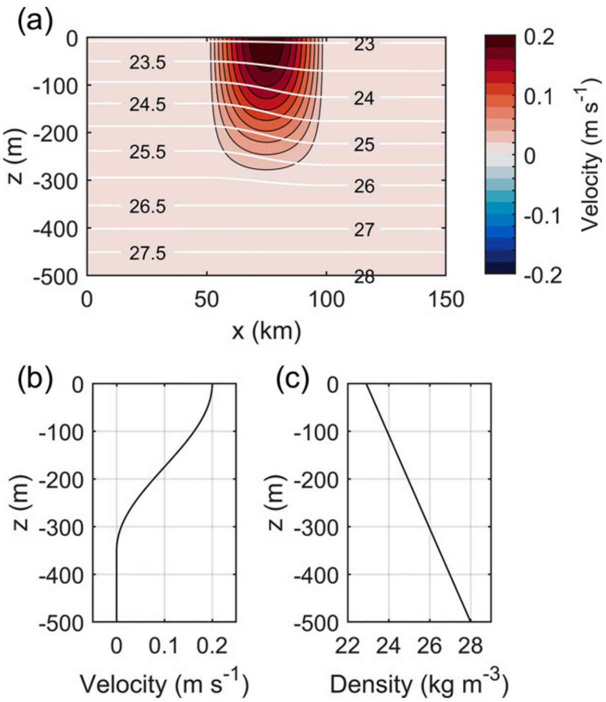

FIG. 4. (a) Vertical section of the along-channel geostrophic velocity (color) overlain by isopycnals (white contours) for the initial state. (b),(c) Vertical profiles of the initial geostrophic velocity and density at $x = 75$ km.

Ekman pumping $w_E(x, t)$ from Eq. (14), the vertical velocity $w(x, z, t)$ from Eqs. (13) and (15), the density $\rho(x, z, t)$ from Eq. (6), and the geostrophic velocity $\upsilon_g(x, z, t)$ from Eq. (11).

4. Comparison between the analytical and numerical solutions: Case study

In this section, the QG model and the idealized numerical model are applied to study the evolution of an initially surface-intensified, laterally sheared geostrophic current (Fig. 4):

$$\upsilon_g(x, z, 0) = \begin{cases} \upsilon_s[\cos(\pi z/H_0) + 1]/2, -H_0 \le z \le 0, \\ 0, -H \le z < -H_0, \end{cases}$$

with

$$\upsilon_s(x, 0) = \begin{cases} 0,\ 0 \le x < l,\ 2l < x \le 3l, \\ V_m \sin[\pi(x - l)/l],\ l \le x \le 2l, \end{cases}$$

where $l = B/3$, and V_m is the maximum value of the initial surface velocity. The initial density is set to accommodate the geostrophic velocity according to the thermal wind relation. The vertical profile of density at the center of the channel is given by

$$\rho(B/2, z, 0) = \rho_b - \left(\rho_0 N^2/g\right)(z + H),$$

where ρ_b is the bottom density. With such initial conditions, $\partial \upsilon_g/\partial z$ and $\partial \rho/\partial x$ are continuous everywhere.

TABLE 1. Parameters for the case study for both the analytical and numerical models.

Parameter	Value	Unit
Sea ice concentration, α	1	—
Ice–ocean drag coefficient, C_{Di}	5.5×10^{-3}	—
Coriolis parameter, f_0	1.4×10^{-4}	s^{-1}
Reference density, ρ_0	1×10^{3}	kg m^{-3}
Buoyancy frequency, N	0.01	s^{-1}
Gravitational acceleration, g	9.8	m s^{-2}
Depth of initial current, H_0	350	m
Maximum initial velocity, V_m	0.2	m s^{-1}
Channel depth, H	500	m
Channel width, B	150	km
Bottom density, ρ_b	28	kg m^{-3}

Parameters for the case study for both the analytical and numerical models are listed in Table 1. In addition, we set the surface boundary layer depth δ to be 20 m in the analytical model and specify a minimum boundary layer depth of 20 m in the KPP scheme in the numerical model. Using Eq. (A9), the significant height of Ekman pumping H_E is estimated to be 218.5 m.

a. *Evolution of the geostrophic current*

The evolution of the surface geostrophic velocity under the effect of ice–ocean stress acts like a horizontal diffusion of momentum. The diffusion coefficient given by $\overline{V}\mu$ is estimated to be 258.4 m^2 s^{-1} using the parameters in Table 1. As shown in Figs. 5a and 5b, both the analytical and numerical geostrophic currents expand from the center at higher velocity to the west and east at lower velocities. This process is accompanied by the attenuation of the lateral velocity shear. Notably, the surface velocity maximum decays quickly from 0.2 to ~0.1 m s^{-1} (a decline of 50%) in just 10 days and continues to decrease over time. Furthermore, the Ekman pumping induced by ice–ocean stress curl is dominated by the symmetrically distributed Ekman downwelling and upwelling (Figs. 5c,d), which decays over time in response to the attenuation of the surface velocity shear. Note that the analytical solutions are somewhat different from the numerical results. Part of the difference can be attributed to the different treatments of ice–ocean stress. For example, the linear stress [Eq. (17)] used in the analytical model has enlarged the stress curl near the two edges of the current compared to the quadratic form [Eq. (12)]. Thus, the analytical geostrophic current appears to be more expansive than the numerical one (cf. Figs. 5a,b).

The geostrophic velocity in the interior evolves as well. As shown in Fig. 6, a subsurface velocity core is formed in the central channel (between $x = 50$ and 100 km) in both analytical and numerical sections (e.g., Figs. 6e,f). This suggests that the geostrophic current changes from being surface intensified to subsurface intensified due to ice–ocean stress. Figure 7 further shows that the velocity core shifts rapidly from the surface down to a depth of 50 m in the first 10 days and remains in the subsurface thereafter. Such modification of geostrophic velocity is a result of the displacement of isopycnals as

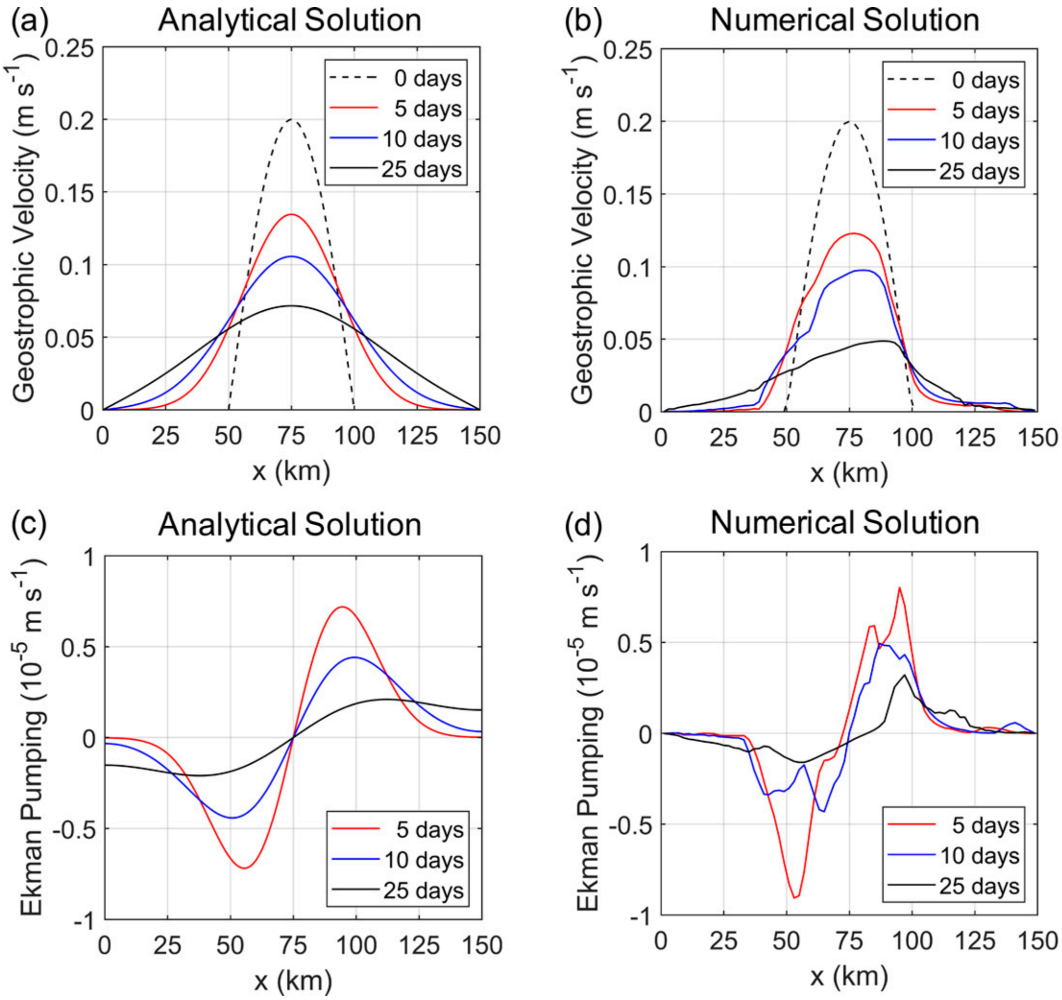

FIG. 5. (a) Analytical and (b) numerical distributions of the surface geostrophic velocity at $t = 0$, 5, 10, and 25 days. (c) Analytical and (d) numerical distributions of the Ekman pumping at $t = 5$, 10, and 25 days.

required by the thermal wind relation [Eq. (8)]. The symmetrically distributed Ekman downwelling and upwelling can set up an overturning to move the isopycnals (downward/upward displacement by downwelling/upwelling), and this then results in a changed thermal wind shear (this is discussed in detail in section 4d). As the velocity maximum deepens, the near-surface isopycnals (e.g., the 23 kg m^{-3} contour) become tilted in the opposite direction to the deeper ones (Fig. 6), and the vertical shear above the velocity maximum turns negative (Fig. 8).

The vertical shear near the bottom is also negative, corresponding to a reversed (southward) flow that extends from the bottom to the middepth (Fig. 6). Note that the analytical reversed flow is relatively steady (Fig. 7a), while the numerical one tends to be more intensive over time (Fig. 7b). This may be a result of the quadratic drag law used in the numerical model, which is stronger near the center of the current. In addition, the analytical section captures two reversed jets near the western and eastern boundaries (e.g., Fig. 6e), but the numerical section does not. This is due to the Ekman pumping in the analytical model expanding more than in the numerical model (see the analysis in the following section).

b. Overturning circulation

The vertical motions in the interior are dominated by the symmetrically distributed downwelling and upwelling as a result of the penetration of Ekman pumping (Fig. 9). In the analytical model, the downwelling/upwelling extends from the center of the channel to the western/eastern boundary (see, e.g., Fig. 9e), in response to the expansion of the surface geostrophic current (Fig. 5a). This produces negative gradient of vertical velocity ($\partial w/\partial x < 0$) near the two side boundaries. According to Eq. (11), $\partial w/\partial x < 0$ requires $\partial(v_g - v_s)/\partial t < 0$, i.e., v_g tends to be more negative over time (note that v_s remains small to accommodate the Dirichlet boundary condition). This is responsible for the formation of the two reversed jets near the western and eastern boundaries in the analytical model (see Fig. 6e).

In the numerical model, the symmetrically distributed downwelling and upwelling are also evident, although there

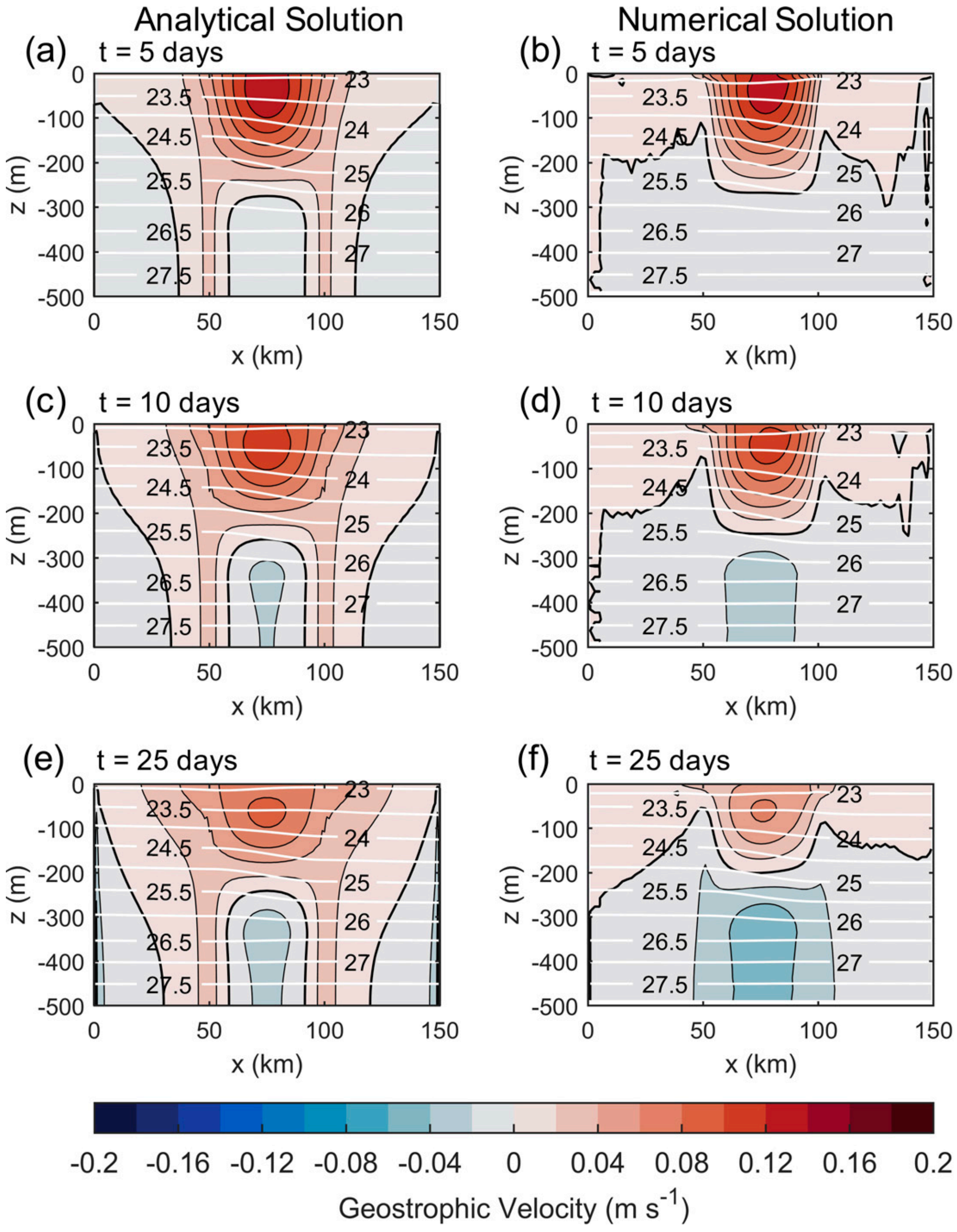

FIG. 6. Vertical sections of the along-channel geostrophic velocity (color) overlain by isopycnals (white contours) at $t = 5$, 10, and 25 days: (left) the analytical solutions and (right) the numerical solutions. Bold black line in each panel shows the zero-velocity contour.

are some other signals with smaller scales (Figs. 9b,d,f). Note that the dominant downwelling and upwelling in the numerical model are not so expansive as in the analytical model. Instead, they appear to be close to each other, residing in the central channel. In this case, there is no reversed jet near the western or eastern boundary (see Figs. 6b,d,f).

Recall the continuity equation $\partial u/\partial x + \partial w/\partial z = 0$. It is appropriate to define a streamfunction ψ that satisfies $u = -\partial\psi/\partial z$ and $w = \partial\psi/\partial x$. Since w is already resolved, we calculate ψ by integrating w along x and deduce u by $-\partial\psi/\partial z$. The resulting streamfunction reveals an anticlockwise overturning circulation, which extends from the surface down to the deep interior (Fig. 10). The

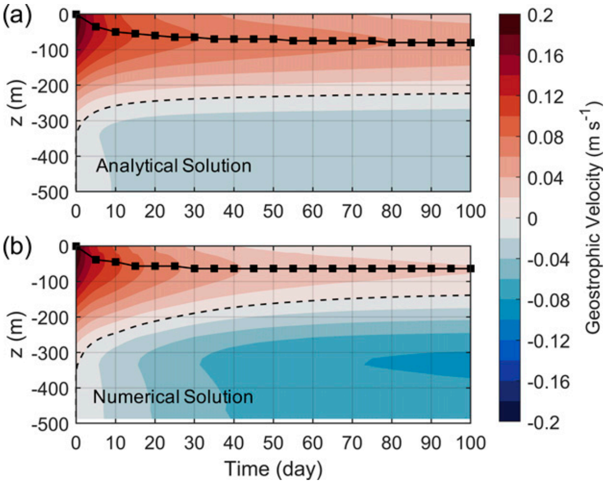

FIG. 7. Depth–time plot of the along-channel geostrophic velocity at $x = 75$ km: (a) the analytical solution and (b) the numerical solution. The solid black line (with squares) indicates the velocity maximum. The dashed black line is the zero-velocity contour.

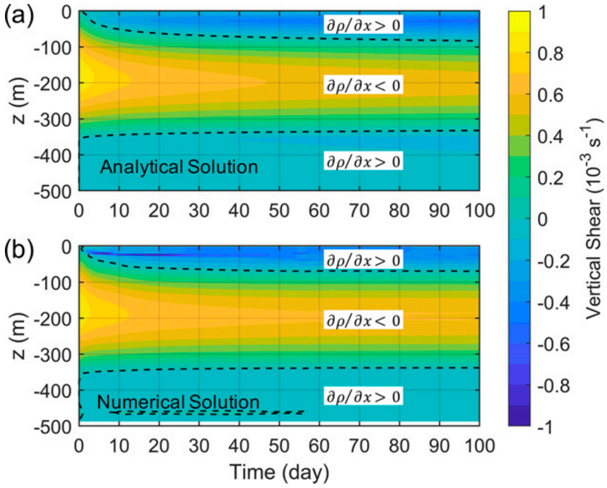

FIG. 8. Depth–time plot of the vertical shear at $x = 75$ km: (a) the analytical solution and (b) the numerical solution. The black dashed lines show the zero-shear contours.

upper arm of the overturning is westward, confined in the surface boundary layer, and fed by the stress-induced Ekman flow (see Figs. 11a,b for the zonal velocity). In the interior, the eastward velocity is much weaker but spans a wider range of depth (Figs. 11c,d). The depth-integrated westward transport in the surface boundary layer (approximately the Ekman transport) is equal to the eastward transport in the interior.

Ideally, the zonal velocity in the interior should be balanced by the local acceleration as suggested by Eq. (2), i.e., $u = -(\partial v_g/\partial t)/f_0$. However, Fig. 11c shows that the analytical output of $-(\partial v_g/\partial t)/f_0$ is weaker than the analytical output of u at $x = 75$ km. This is the limitation of the analytical solution. Recall that the analytical v_s is obtained by solving the evolution Eq. (18), which uses the linear ice–ocean stress and assumes a constant significant height of Ekman pumping H_E (see the appendix). Note, however, H_E should be time and space dependent because w_E has different modes as it evolves, although the second mode remains dominant. The assumption that H_E is constant has greatly simplified the equation but inevitably introduced errors into the final results. On the one hand, the analytical solution underestimates $\partial w/\partial x$ near the center of the channel compared to the numerical result and thus underestimates $\partial v_s/\partial t$ and $\partial v_g/\partial t$ [according to Eqs. (10) and (11)]. On the other hand, there is too much Ekman transport in the surface boundary layer that is further circulated in the overturning to feed the interior eastward transport, leading to an overestimate of the zonal velocity. Consequently, $-(\partial v_g/\partial t)/f_0$ is weaker than u as seen in Fig. 11c. In the numerical model, $-(\partial v_g/\partial t)/f_0$ and u are approximately balanced (Fig. 11d), suggesting that the QG approximation [e.g., Eq. (2)] is reasonable.

c. *Scaling*

From the QG omega equation [Eq. (5)], we derive a scaling for the depth from which waters are drawn up to the surface by the overturning circulation, $D = (f_0L)/N$ (L is the horizontal length scale of the flow). Using the parameters in Table 1, D is estimated to be 334.2 m. Thus, the overturning could reach the bottom over the shelf (e.g., the Chukchi shelf). In the appendix we also derive a scaling for the significant height of Ekman pumping H_E, which characterizes the depth to which the indirect effect of Ekman pumping is felt. Note that the vertical velocity w in the interior is due to the penetration of Ekman pumping and the streamfunction of overturning circulation is an integral of w along x. Therefore, H_E is of the same vertical length scale as the overturning. It is also noted that the penetration of Ekman pumping is limited by the finite bottom depth H by a coefficient $\{\cosh[(H-\delta)/D]-1\}/\sinh[(H-\delta)/D]$ ranging between 0 and 1. In the extreme case where the channel is infinite deep ($H \rightarrow +\infty$), the coefficient approaches 1 and H_E is equivalent to D. With $H_E = O(f_0L/N)$ the scale of the parameter μ in Eq. (18) can be expressed as the horizontal length scale of the flow L times $\alpha C_{Di}N/f_0$, i.e., $\mu = O(\alpha C_{Di}NL/f_0)$. For typical parameters, $\mu = O(L)$ but it could be larger for weaker stratification.

The time scale for the evolution of the geostrophic current due to uneven ice–ocean stress is derived from Eq. (18) and is of the form $T = f_0L/(\alpha C_{Di}NV)$, where V is the velocity scale. For the case $V = 0.1$ m s^{-1}, T is approximately 7 days. This scaling characterizes the time for the lateral expansion of the surface geostrophic current and the decay of the strength of the velocity core. Although $T \approx 7$ days is a linear estimate, it is generally consistent with the resolved time evolution [e.g., in Fig. 7, the strength of the velocity core decays over $O(10)$ days]. Note also that T is much larger than the time scale for the geostrophic adjustment ($1/f_0 \approx 2$ h), and thus the temporal Rossby number $1/(f_0T)$ is small. This is required by the QG theory.

d. *Mechanism for the overturning-induced modification of the geostrophic current*

In light of the analytical and numerical results, we propose a mechanism of how the overturning circulation modifies the

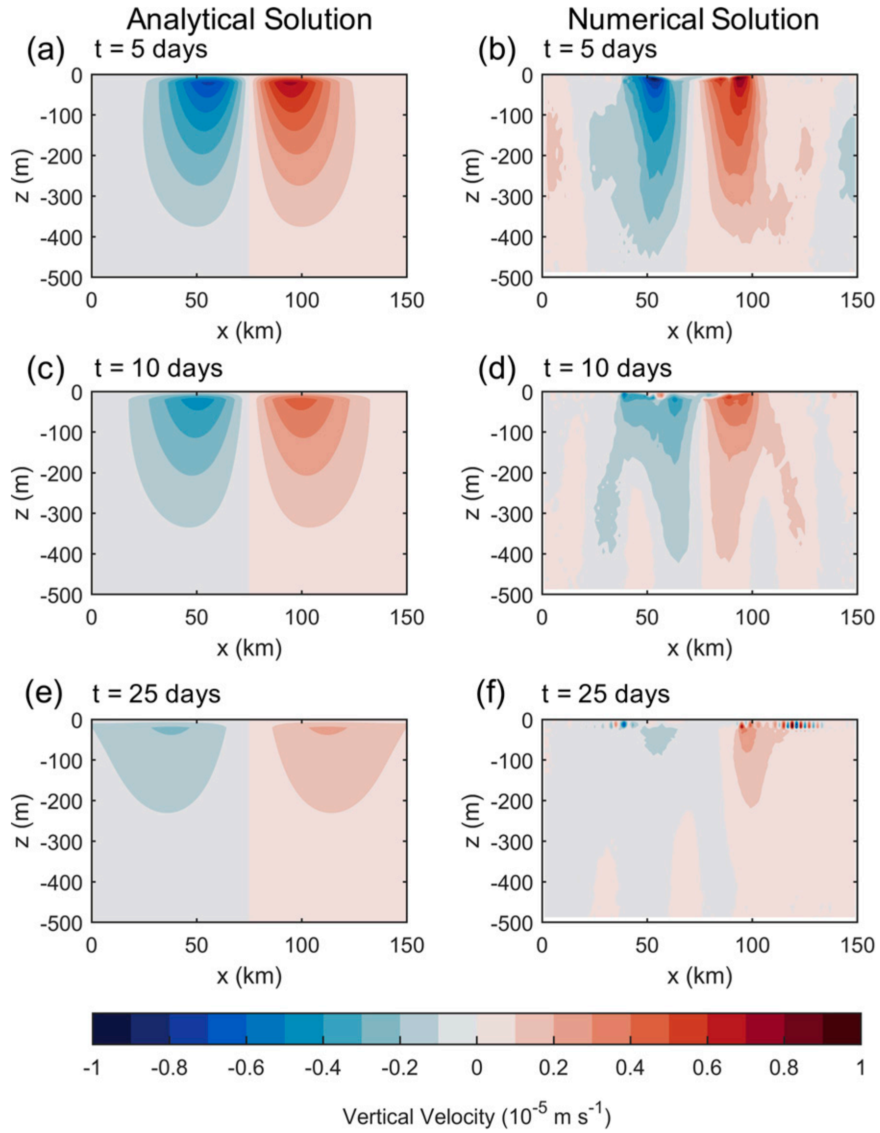

FIG. 9. Vertical sections of the vertical velocity at $t = 5$, 10, and 25 days: (left) the analytical solutions and (right) the numerical solutions.

geostrophic velocity and density structures. Consider the case that the geostrophic current is initially surface intensified and laterally sheared, which extends down to a depth at and below which the isopycnal slope is zero (Fig. 12). The presence of the overturning circulation can cause the displacement of isopycnals as suggested by Eq. (6). Specifically, the downwelling component ($w < 0$) of the overturning means a downward advection of light water, which moves isopycnals downward and results in the decline in local density ($\partial\rho/\partial t < 0$). In contrast, the upwelling component ($w > 0$) of the overturning transports heavy water upward. This causes the upward displacement of isopycnals and the increase in local density ($\partial\rho/\partial t > 0$). Note that the vertical velocity near the base of the surface boundary layer is approximately the Ekman pumping, which is large enough to reverse the tilt of the near-surface isopycnal ($\partial\rho/\partial x$ changes from being negative to positive). At a deeper depth the vertical velocity is smaller and the isopycnal is steeper. In this case, the isopycnal tilt can hardly be reversed, i.e., $\partial\rho/\partial x$ remains negative. Accordingly, there must be a critical depth at which the isopycnal slope is zero ($\partial\rho/\partial x = 0$) and the geostrophic velocity reaches a maximum ($\partial v_g/\partial z = 0$). This explains the formation of the subsurface velocity core in the analytical and numerical sections (see, e.g., Figs. 6e,f).

It is also worth noting that, in the initial state, the near-bottom isopycnal is horizontal and is easily tilted by even weak vertical velocity. As the near-bottom isopycnal is forced by the overturning to rotate anticlockwise slightly, the corresponding vertical shear turns negative ($\partial v_g/\partial z < 0$). Consequently, a reversed flow that extends from the bottom to the

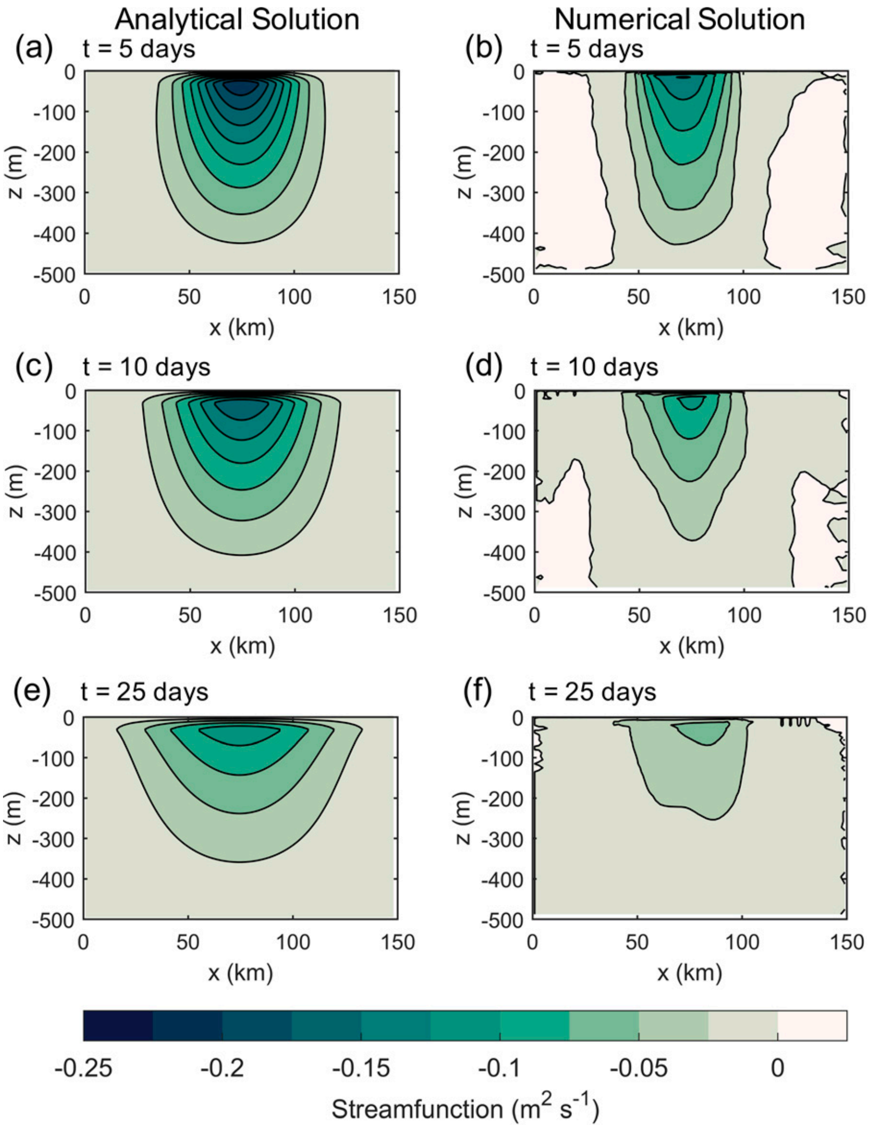

FIG. 10. Vertical sections of the overturning streamfunction at t = 5, 10, and 25 days: (left) the analytical solutions and (right) the numerical solutions.

middepth is generated. As noted above in section 4a, the reversed flow in the numerical model tends to be more intensive over time. This should be due to the overturning circulation that resides in the central channel (Figs. 10b,d,f), rather than expanding toward the western and eastern boundaries as in the analytical model (Figs. 10a,c,e).

5. Summary and discussion

In this study, we have established a simple theoretical framework based on a QG model to study the temporal evolution of a geostrophic current under sea ice. By solving the QG omega equation and a derived evolution equation, we obtained analytical solutions for the vertical velocity (as a function of Ekman pumping) and the evolving geostrophic velocity. These solutions are also supported by the results from an idealized numerical model.

The main finding in this work is that the uneven stress between the ice and an initially surface-intensified, laterally sheared geostrophic current can produce an overturning circulation to trigger the displacement of isopycnals and modify the vertical structure of the geostrophic velocity. As the near-surface isopycnals are forced to be tilted in the opposite direction to the deeper ones, a subsurface velocity core is thus generated (via geostrophic setup). This mechanism should help understand the formation of the subsurface velocity core in the Chukchi Slope Current (Li et al. 2019). In addition, our solutions show that the subsurface velocity core is present in the steady state (see Fig. 7, the velocity maximum remains in the subsurface to the end of calculation), suggesting the

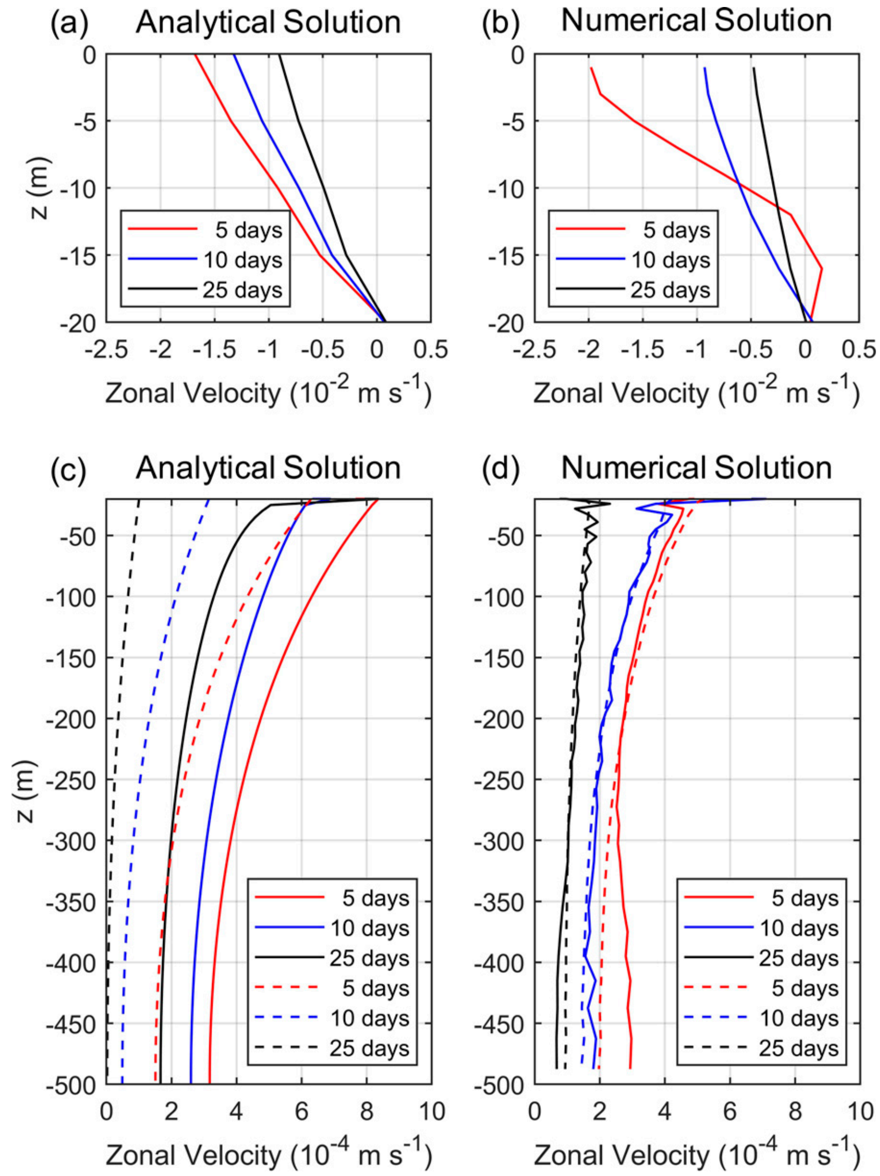

FIG. 11. Vertical profiles of zonal velocity (solid lines) at $x = 75$ km at $t = 5$, 10, and 25 days: (a),(b) in the surface boundary layer and (c),(d) in the interior. Panels (a) and (c) are deduced from the analytical overturning streamfunction by $u = -\partial\psi/\partial z$ and (b) and (d) are from the numerical output. The dashed lines in (c) and (d) indicate the vertical profiles of $-(\partial v_g/\partial t)/f_0$.

persistence of the subsurface current under sea ice (if not affected by other forcings). This is consistent with the observational result that the subsurface slope current is present through winter and spring (Li et al. 2019) when the Chukchi slope region is covered by sea ice.

Our analytical and numerical solutions also capture a reversed flow extending from the bottom to the middepth, implying that the effect of ice–ocean stress is not limited to the upper ocean. Recent shipboard and mooring observations have shown the presence of a southeastward current residing on the midslope of Chukchi Sea, beneath the northwestward Chukchi Slope Current (Corlett and Pickart 2017; Li et al. 2019; Stabeno and McCabe 2020). This current is known to be the onshore branch of the Atlantic Water boundary current system in the western Arctic Ocean, which advects the Atlantic Water emanating from the Chukchi Gap, with a contribution from an interior branch through the Chukchi Borderland (Li et al. 2020). Since the subsurface velocity core in the slope current is likely to be related to sea ice, it would be instructive to consider the response of the Atlantic Water boundary current to the interaction between the ice and the slope current in the future work.

The Chukchi Slope Current is flowing along the continental slope with its onshore part reaching the bottom topography

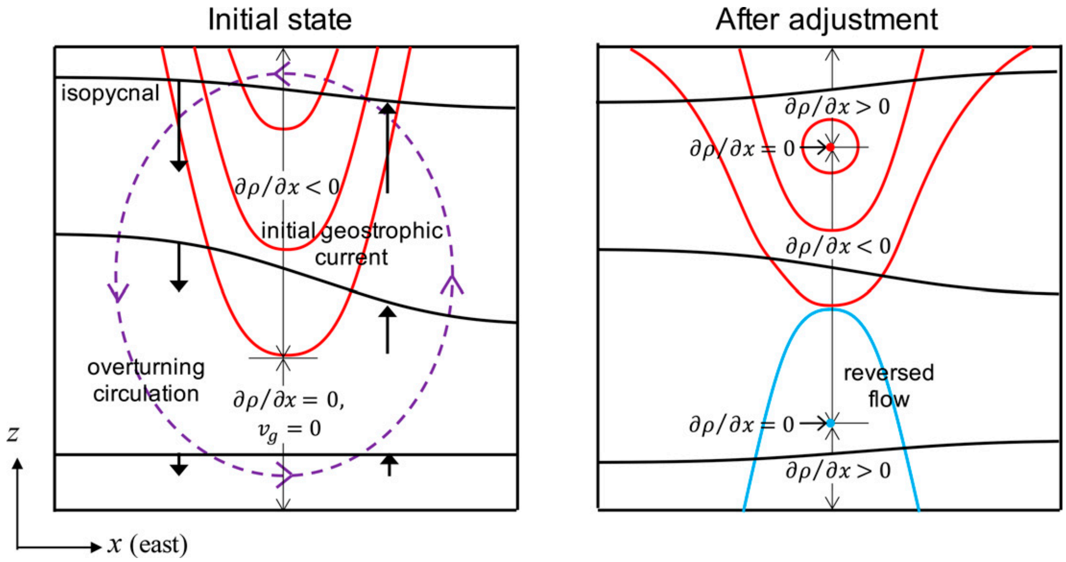

FIG. 12. Schematic describing the adjustment of the geostrophic velocity and density structures induced by the overturning circulation.

(Corlett and Pickart 2017; Li et al. 2019). Therefore, the bottom slope and friction are likely to influence the modification of the slope current triggered by uneven ice–ocean stress. This is the case in our idealized numerical model. For example, when the model considers bottom friction, the reversed flow is weakened and does not extend upward so much as in the slip-bottom case. Furthermore, when a bottom slope is introduced, the overturning can reach the slope and result in a reversed flow spanning from the shelf break offshore to the deep region (not shown). This suggests that the ice–ocean stress could potentially enhance the eastward-flowing Chukchi shelfbreak jet, onshore of the slope current.

The overturning circulation induced by the uneven ice–ocean stress might affect the shelf–basin exchange. Specifically, the overturning on the Chukchi shelf break and slope should be able to reduce the wind-driven off-shelf transport in the surface boundary layer and enhance the off-shelf transport in deeper layers. As such, the overturning redistributes the cross-shelf velocity in the vertical. On the other hand, the upwelling component of the overturning is likely to transport nutrient-rich subsurface water upward to the surface and cause the under-ice phytoplankton blooms. Many observations have shown that the under-ice production is significant on a pan-Arctic scale over the past two decades, which would become increasingly important in future marine Arctic biogeochemical cycles (Ardyna et al. 2020). Further work is needed to investigate the role of the under-ice overturning circulation in the transport of volume, heat, freshwater, and nutrients.

Acknowledgments. This work was funded by the National Key Research and Development Program of China (Grant 2017YFA0604600), the National Natural Science Foundation of China (Grant 41676019), the Fundamental Research Funds for the Central Universities (Grant 2019B81214), the Postgraduate Research and Practice Innovation Program of Jiangsu Province (Grant KYCX19_0384), and the National Science Foundation (MAS, Grants OPP-1822334, OCE-2122633). We thank the editor and reviewers for their helpful comments and suggestions.

Data availability statement. The numerical model configuration, parameters, forcing fields, and representative model output are stored at https://doi.org/10.5281/zenodo.5606478.

APPENDIX

The Derivation of the Evolution Equation for the Surface Geostrophic Current under Sea Ice

If we define the significant height of Ekman pumping by

$$H_E = \frac{\int_{-\infty}^{0} w\,dz}{w_E}, \qquad \text{(A1)}$$

Eq. (9) can be rewritten as

$$\frac{\partial v_s}{\partial t} = -\frac{N^2 H_E}{f_0}\frac{\partial w_E}{\partial x}. \qquad \text{(A2)}$$

Integrating w over $-H \le z \le 0$ using Eqs. (12) and (14) gives

$$\int_{-\delta}^{0} w(x,z)dz = \frac{1}{2}\left(\pi - 1 - e^{-\pi/2}\right)D_E w_E \approx D_E w_E \qquad \text{(A3)}$$

and

$$\int_{-H}^{-\delta} w(x,z)dz = \sum_{k=1}^{\infty} a_k \frac{f_0 B}{k\pi N}\left\{\cosh\left[\frac{k\pi N}{f_0 B}(H-\delta) - 1\right]\right\}\sin\left(\frac{k\pi}{B}x\right), \qquad \text{(A4)}$$

where the coefficient a_k ($k = 1, 2, 3, \ldots$) is determined by Ekman pumping:

$$a_k = \frac{2}{B\sinh\left[\frac{k\pi N}{f_0 B}(H-\delta)\right]}\int_0^B w_E(x)\sin\left(\frac{k\pi}{B}x\right)dx. \tag{A5}$$

Suppose that the Ekman pumping can be written as a linear combination of different modes:

$$w_E = \sum_{n=1}^{\infty} M_n \sin\left(\frac{n\pi}{B}x\right), \tag{A6}$$

where M_n ($n = 1, 2, 3, \ldots$) represents the significance of each mode. For the case that the Ekman pumping is driven by the ice–ocean stress, the second mode should be the most significant (downwelling west of $x = B/2$ and upwelling east of $x = B/2$), i.e., $|M_2| \gg |M_n|$, $n \neq 2$, and

$$w_E \approx M_2 \sin\left(\frac{2\pi}{B}x\right), \tag{A7}$$

with a length scale of $L = B/(2\pi)$. Substitution of Eq. (A7) into Eq. (A5) yields

$$a_2 = \frac{M_2}{\sinh\left[\frac{N}{f_0 L}(H-\delta)\right]}$$

and a_k ($k \neq 2$) = 0. Thus, Eq. (A4) becomes

$$\int_{-H}^{-\delta} w(x,z)dz = \frac{f_0 L}{N}\frac{\cosh\left[\frac{N}{f_0 L}(H-\delta)\right]-1}{\sinh\left[\frac{N}{f_0 L}(H-\delta)\right]}w_E. \tag{A8}$$

By combining Eqs. (A3) and (A8), we have

$$H_E \approx D_E + \frac{f_0 L}{N}\frac{\cosh\left[\frac{N}{f_0 L}(H-\delta)\right]-1}{\sinh\left[\frac{N}{f_0 L}(H-\delta)\right]}. \tag{A9}$$

Note that H_E is constrained by the channel depth H. As $H \to +\infty$, H_E approaches $D_E + f_0 L/N$, implying that the less (more) stratified ocean is more (less) likely to be penetrated by Ekman pumping. Using the quadratic ice–ocean stress ($\tau^y = -\alpha\rho_0 C_{Di} v_s^2$), the Ekman pumping can be expressed by

$$w_E = -\frac{\alpha C_{Di}}{f_0}\frac{\partial v_s^2}{\partial x}, \tag{A10}$$

then, Eq. (A2) becomes

$$\frac{\partial v_s}{\partial t} - \mu\frac{\partial^2 v_s^2}{\partial x^2} = 0, \tag{A11}$$

where $\mu = \alpha C_{Di} N^2 H_E / f_0^2$ is a parameter. It is difficult to find an accurate analytical solution to Eq. (A11) because of the presence of the nonlinear term associated with the quadratic ice–ocean stress. To linearize Eq. (A11), we replace τ^y with a linear stress $\hat{\tau}^y = -\alpha\rho_0 \hat{C}_{Di} v_s$, where $\hat{C}_{Di}$ is the drag coefficient. It is appropriate to take $\hat{C}_{Di}$ to be equal to $C_{Di}\overline{V}$ ($\overline{V}$ is the zonal average of the initial surface velocity) so that $\hat{\tau}^y$ is of the same order as τ^y. Then, Eq. (A11) reduces to a solvable linear evolution equation:

$$\frac{\partial v_s}{\partial t} - \overline{V}\mu\frac{\partial^2 v_s}{\partial x^2} = 0, \tag{A12}$$

which is of the same form as the heat (or diffusion) equation.

REFERENCES

Ardyna, M., and Coauthors, 2020: Under-ice phytoplankton blooms: Shedding light on the "invisible" part of Arctic primary production. *Front. Mar. Sci.*, **7**, 608032, https://doi.org/10.3389/fmars.2020.608032.

Boury, S., and Coauthors, 2020: Whither the Chukchi Slope Current? *J. Phys. Oceanogr.*, **50**, 1717–1732, https://doi.org/10.1175/JPO-D-19-0273.1.

Corlett, W. B., and R. S. Pickart, 2017: The Chukchi Slope Current. *Prog. Oceanogr.*, **153**, 50–65, https://doi.org/10.1016/j.pocean.2017.04.005.

Doddridge, E. W., G. Meneghello, J. Marshall, J. Scott, and C. Lique, 2019: A three-way balance in the Beaufort Gyre: The ice-ocean governor, wind stress, and eddy diffusivity. *J. Geophys. Res. Oceans*, **124**, 3107–3124, https://doi.org/10.1029/2018JC014897.

Fox-Kemper, B., and D. Menemenlis, 2008: Can large eddy simulation techniques improve mesoscale rich ocean models? *Ocean Modeling in an Eddying Regime*, *Geophys. Monogr.*, Vol. 177, Amer. Geophys. Union, 319–337.

Hoskins, B. J., I. Draghici, and H. C. Davies, 1978: A new look at the ω-equation. *Quart. J. Roy. Meteor. Soc.*, **104**, 31–38, https://doi.org/10.1002/qj.49710443903.

Itoh, M., S. Nishino, Y. Kawaguchi, and T. Kikuchi, 2013: Barrow Canyon volume, heat, and freshwater fluxes revealed by long-term mooring observations between 2000 and 2008. *J. Geophys. Res. Oceans*, **118**, 4363–4379, https://doi.org/10.1002/jgrc.20290.

Jackett, D. R., and T. J. McDougall, 1995: Minimal adjustment of hydrographic profiles to achieve static stability. *J. Atmos. Oceanic Technol.*, **12**, 381–389, https://doi.org/10.1175/1520-0426(1995)012<0381:MAOHPT>2.0.CO;2.

Large, W., J. McWilliams, and S. Doney, 1994: Oceanic vertical mixing: A review and a model with nonlocal boundary layer parameterization. *Rev. Geophys.*, **32**, 363–403, https://doi.org/10.1029/94RG01872.

Leith, C. E., 1996: Stochastic models of chaotic systems. *Physica D*, **98**, 481–491, https://doi.org/10.1016/0167-2789(96)00107-8.

Leng, H., M. A. Spall, R. S. Pickart, P. Lin, and X. Bai, 2021: Origin and fate of the Chukchi Slope Current using a numerical model and in-situ data. *J. Geophys. Res. Oceans*, **126**, e2021JC017291, https://doi.org/10.1029/2021JC017291.

Li, J., R. S. Pickart, P. Lin, F. Bahr, K. R. Arrigo, L. Juranek, and X.-Y. Yang, 2020: The Atlantic water boundary current in the Chukchi Borderland and southern Canada Basin. *J. Geophys. Res. Oceans*, **125**, e2020JC016197, https://doi.org/10.1029/2020JC016197.

Li, M., R. S. Pickart, M. A. Spall, T. J. Weingartner, P. Lin, G. W. K. Moore, and Y. Qig, 2019: Circulation of the Chukchi Sea shelfbreak and slope from moored timeseries. *Prog. Oceanogr.*, **172**, 14–33, https://doi.org/10.1016/j.pocean.2019.01.002.

Lin, P., and Coauthors, 2020: Circulation in the vicinity of Mackenzie Canyon from a year-long mooring array. *Prog. Oceanogr.*, **187**, 102396, https://doi.org/10.1016/j.pocean.2020.102396.

Losch, M., D. Menemenlis, P. Heimbach, J.-M. Campin, and C. Hill, 2010: On the formulation of sea-ice models. Part 1: Effects of different solver implementations and parameterizations. *Ocean Modell.*, **33**, 129–144, https://doi.org/10.1016/j.ocemod.2009.12.008.

Marshall, J., C. Hill, L. Perelman, and A. Adcroft, 1997: Hydrostatic, quasi-hydrostatic and non-hydrostatic ocean modeling. *J. Geophys. Res.*, **102**, 5733–5752, https://doi.org/10.1029/96JC02776.

Meneghello, G., J. C. Marshall, J.-M. Campin, E. Doddridge, and M.-L. Timmermans, 2018a: The ice-ocean governor: Ice-ocean stress feedback limits Beaufort Gyre spin-up. *Geophys. Res. Lett.*, **45**, 11 293–11 299, https://doi.org/10.1029/2018GL080171.

——, ——, M.-L. Timmermans, and J. Scott, 2018b: Observations of seasonal upwelling and downwelling in the Beaufort Sea mediated by sea ice. *J. Phys. Oceanogr.*, **48**, 795–805, https://doi.org/10.1175/JPO-D-17-0188.1.

——, E. Doddridge, J. Marshall, J. Scott, and J.-M. Campin, 2020: Exploring the role of the “ice–ocean governor” and mesoscale eddies in the equilibration of the Beaufort Gyre: Lessons from observations. *J. Phys. Oceanogr.*, **50**, 269–277, https://doi.org/10.1175/JPO-D-18-0223.1.

——, J. Marshall, C. Lique, P. E. Isachsen, E. Doddridge, J.-M. Campin, H. Regan, and C. Talandier, 2021: Genesis and decay of mesoscale baroclinic eddies in the seasonally ice-covered interior Arctic Ocean. *J. Phys. Oceanogr.*, **51**, 115–129, https://doi.org/10.1175/JPO-D-20-0054.1.

Nikolopoulos, A., R. S. Pickart, P. S. Fratantoni, K. Shimada, D. J. Torres, and E. P. Jones, 2009: The western Arctic boundary current at 152°W: Structure, variability, and transport. *Deep-Sea Res. II*, **56**, 1164–1181, https://doi.org/10.1016/j.dsr2.2008.10.014.

Spall, M., R. S. Pickart, M. Li, M. Itoh, P. Lin, T. Kikuchi, and Y. Qi, 2018: Transport of Pacific water into the Canada basin and the formation of the Chukchi Slope Current. *J. Geophys. Res. Oceans*, **123**, 7453–7471, https://doi.org/10.1029/2018JC013825.

Stabeno, P. J., and R. M. McCabe, 2020: Vertical structure and temporal variability of currents over the Chukchi Sea continental slope. *Deep-Sea Res. II*, **177**, 104805, https://doi.org/10.1016/j.dsr2.2020.104805.

Wang, Q., J. Marshall, J. Scott, G. Meneghello, S. Danilov, and T. Jung, 2019: On the feedback of ice–ocean stress coupling from geostrophic currents in an anticyclonic wind regime over the Beaufort Gyre. *J. Phys. Oceanogr.*, **49**, 369–383, https://doi.org/10.1175/JPO-D-18-0185.1.

Watanabe, E., J. Onodera, M. Itoh, S. Nishino, and T. Kikuchi, 2017: Winter transport of subsurface warm water toward the Arctic Chukchi Borderland. *Deep-Sea Res. I*, **128**, 115–130, https://doi.org/10.1016/j.dsr.2017.08.009.

Weingartner, T. J., R. A. Potter, C. A. Stoudt, E. L. Dobbins, H. Statscewich, P. R. Winsor, T. D. Mudge, and K. Borg, 2017: Transport and thermohaline variability in Barrow Canyon on the northeastern Chukchi Sea shelf. *J. Geophys. Res. Oceans*, **122**, 3565–3585, https://doi.org/10.1002/2016JC012636.

Zhang, J., and W. D. Hibler, 1997: On an efficient numerical method for modeling sea ice dynamics. *J. Geophys. Res.*, **102**, 8691–8702, https://doi.org/10.1029/96JC03744.